

Hydrothermal synthesis and complete phase diagram of $\text{FeSe}_{1-x}\text{S}_x$ ($0 \leq x \leq 1$) single crystals

Xiaolei Yi,¹ Xiangzhuo Xing,^{1,*} Lingyao Qin,¹ Jiajia Feng,¹ Meng Li,¹
Yufeng Zhang,¹ Yan Meng,¹ Nan Zhou,¹ Yue Sun,^{2,†} and Zhixiang Shi^{1,‡}

¹*School of Physics, Southeast University, Nanjing 211189, China*

²*Department of Physics and Mathematics, Aoyama Gakuin University, Sagami-hara 252-5258, Japan*

(Dated: December 22, 2024)

We report the successful synthesis of $\text{FeSe}_{1-x}\text{S}_x$ single crystals with x ranging from 0 to 1 via a hydrothermal method. A complete phase diagram of $\text{FeSe}_{1-x}\text{S}_x$ has been obtained based on resistivity and magnetization measurements. The nematicity is suppressed with increasing x , and a small superconducting dome appears within the nematic phase. Outside the nematic phase, the superconductivity is continuously suppressed and reaches a minimum T_c at $x = 0.45$; beyond this point, T_c slowly increases until $x = 1$. Intriguingly, an anomalous resistivity upturn with a characteristic temperature T^* in the intermediate region of $0.31 \leq x \leq 0.71$ is observed. T^* shows a dome-like behavior with a maximum value at $x = 0.45$, which is opposite to the evolution of T_c , indicating competition between T^* and superconductivity. The origin of T^* is discussed in terms of weak localization effects or a possible magnetic transition. Furthermore, the normal state resistivity evolves from non-Fermi-liquid to Fermi-liquid behavior with S doping at low temperatures, accompanied by a reduction in electronic correlations. Our study addresses the lack of single crystals in the high-S doping region and provides a complete phase diagram, which will promote the study of relations between nematicity, superconductivity, and magnetism.

I. INTRODUCTION

The discovery of superconductivity in iron-based superconductors (IBSs) [1] has opened a new era in the search for high-temperature superconductors and in research on the mechanisms governing unconventional superconductivity. The iron chalcogenide superconductor FeSe [2], which exhibits the simplest crystal structure among IBSs, has attracted considerable interest due to its unique properties [3]. FeSe is a compensated semimetal that exhibits superconductivity with a superconducting (SC) transition temperature $T_c \sim 9$ K at ambient pressure [2]. Intriguingly, T_c can be increased to 37 K by the application of pressure [4], to values exceeding 40 K through intercalation [5], ionic liquid gating [6], and potassium deposition [7]. More surprisingly, signs of superconductivity with a T_c exceeding 65 K have also been observed in a monolayer FeSe film on a SrTiO_3 substrate [8, 9]. Because the Fermi energies are extremely small and comparable to the SC gap, the superconductivity in bulk FeSe has been argued to be close to a Bardeen-Cooper-Schrieffer/Bose-Einstein-condensation (BEC) crossover [10]. Unlike other IBSs, FeSe undergoes a structural (nematic) transition at $T_s \sim 87$ K without a magnetic transition [3, 11–14]. Therefore, FeSe is a fascinating platform for investigating the interplay between nematicity and superconductivity.

Isovalent S substitution, which maintains the nature of compensated semimetals, is a clean and effective route

for tuning the ground state and electronic interactions in FeSe. It has been reported that the nematic order is gradually suppressed by S doping in $\text{FeSe}_{1-x}\text{S}_x$ [14–18], and a non-magnetic nematic quantum critical point (QCP) appears at $x \sim 0.17$ [19]. Nuclear magnetic resonance (NMR) measurements have revealed that antiferromagnetic (AFM) fluctuations are slightly enhanced and then strongly suppressed with S substitution, leading to negligible AFM fluctuations near the QCP [16]. The nematic QCP has a significant impact on both the SC [19, 20] and normal state properties [21–23]. The SC gap exhibits an abrupt change across the nematic QCP [19]. Within the nematic phase, the small gap is highly anisotropic with deep minima or nodes, while the large gap is more isotropic [19, 24–27]. By contrast, the larger gap becomes strongly anisotropic outside the nematic phase [19, 20]. Meanwhile, the normal state resistivity in the vicinity of the QCP exhibits T -linear behavior at low temperatures [21–23, 28], signifying non-Fermi-liquid behavior due to the nematic critical fluctuation. Moreover, quantum oscillation measurements have indicated a topological Lifshitz transition and a reduction in electronic correlations across the nematic QCP [17].

Thus far, although increasingly more peculiarities of $\text{FeSe}_{1-x}\text{S}_x$ have been revealed, very few studies have reported on the high-S doping region due to difficulties in synthesizing $\text{FeSe}_{1-x}\text{S}_x$ single crystals with $x > 0.29$ by chemical vapor transport (CVT). Recently, Nabeshima *et al.* reported the growth of $\text{FeSe}_{1-x}\text{S}_x$ thin films up to $x = 0.43$ [29]. However, these thin films show some differences from CVT-grown single crystals, possibly due to the lattice strain effect. To get deeper insights into the evolution of intrinsic bulk properties, the synthesis of $\text{FeSe}_{1-x}\text{S}_x$ single crystals with a higher S content ($x > 0.29$) is highly desirable.

* xzxing@seu.edu.cn

† sunyue@phys.aoyama.ac.jp

‡ zxshi@seu.edu.cn

In this paper, we report the successful synthesis of a series of $\text{FeSe}_{1-x}\text{S}_x$ single crystals with S content covering the full range ($0 \leq x \leq 1$). The single crystals were produced by a hydrothermal method, which enabled us to obtain a complete doping phase diagram. We find that the phase diagram in the low-S doping region agrees with that established from CVT-grown single crystals. Outside the nematic phase, the superconductivity is continuously suppressed and reaches a minimum $T_c = 2.8$ K at $x = 0.45$; beyond this point, T_c slowly increases toward that of FeS. Remarkably, an anomalous resistivity upturn above T_c is observed with a characteristic temperature T^* , which exhibits a dome-shaped dependence on S content and a maximum value at $x = 0.45$, indicating competition between T_c and T^* . Furthermore, the normal state resistivity evolves from non-Fermi-liquid to Fermi-liquid behavior with S doping at low temperatures, accompanied by a reduction in electronic correlations.

II. EXPERIMENTAL DETAILS

$\text{FeSe}_{1-x}\text{S}_x$ single crystals were synthesized by deintercalation of K ions from $\text{K}_{0.8}\text{Fe}_{1.6}\text{Se}_{2-x}\text{S}_x$ precursors using a hydrothermal ion-release/introduction technique [30, 31], as depicted by a schematic diagram in Fig. 1(a). First, $\text{K}_{0.8}\text{Fe}_{1.6}\text{Se}_{2-x}\text{S}_x$ single crystals were synthesized by a self-flux method as described in the Supplementary Material [32]. For the hydrothermal reactions, a given amount of NaOH was dissolved in 10 mL deionized water in a Teflon-lined stainless steel autoclave (25 mL). Then, Fe powder, selenourea, thiourea, and several pieces of $\text{K}_{0.8}\text{Fe}_{1.6}\text{Se}_{2-x}\text{S}_x$ single crystals were added to the solution. Details regarding the quantities of starting materials for the different $\text{FeSe}_{1-x}\text{S}_x$ single crystals are given in Table S1 [32]. The autoclave was tightly sealed, heated to 403–423 K, and maintained for 50–70 h. $\text{FeSe}_{1-x}\text{S}_x$ single crystals were finally obtained by washing the products with deionized water and were found to be almost identical to the $\text{K}_{0.8}\text{Fe}_{1.6}\text{Se}_{2-x}\text{S}_x$ precursors in shape and size, as shown in Fig. 1(b).

Single-crystal X-ray diffraction (XRD) measurements were performed at room temperature on a commercial Rigaku diffractometer with Cu $K\alpha$ radiation, and elemental analysis was performed by a scanning electron microscope equipped with an energy dispersive X-ray (EDX) spectroscopy probe. Electrical transport measurements were performed on a physical property measurement system (PPMS-9T, Quantum Design). Magnetization measurements were also performed on a physical property measurement system (PPMS-9T, Quantum Design) with a vibrating sample magnetometer attachment.

III. RESULTS AND DISCUSSION

The actual S content of the obtained $\text{FeSe}_{1-x}\text{S}_x$ single crystals was determined by EDX measurements. Several

representative EDX spectra are presented in Fig. S1 [32]. The results show that no trace of K is detected for any of the single crystals, indicating that the interlayer K ions are completely released from the $\text{K}_{0.8}\text{Fe}_{1.6}\text{Se}_{2-x}\text{S}_x$ precursors. For each single crystal, several different spots were selected in the EDX measurements, and the average was used to determine the actual stoichiometry composition, as listed in Table S1 [32]. Henceforth, we will refer to the single crystals by their actual S content throughout this paper.

Figure 1(c) shows the single-crystal XRD patterns of $\text{FeSe}_{1-x}\text{S}_x$ single crystals with different values of x . As can be seen, only (00 l) peaks are detected, indicating the good c -axis orientation of the obtained single crystals. Meanwhile, all peaks can be well indexed by a tetragonal structure with the space group of $P4/nmm$, in contrast to the case of $\text{K}_{0.8}\text{Fe}_{1.6}\text{Se}_{2-x}\text{S}_x$ with $I4/m$ as shown in Fig. S2(a) [32]. The lattice parameter c as a function of x is shown in Fig. 1(d). The values of c are 5.527 Å and 5.025 Å for FeSe and FeS, respectively, consistent with previous reports [31, 33]. As expected, the lattice parameter c decreases monotonically with increasing x due to the smaller ionic radius of S^{2-} compared with Se^{2-} , indicating that the S atoms are successfully incorporated into the crystal lattice.

Figure 2(a) presents the temperature dependence of the in-plane resistivity $\rho(T)$ normalized to the corresponding value at 300 K for different values of x . For undoped FeSe single crystals, the nematic transition occurs near $T_s \sim 75$ K, as determined from the temperature derivative of resistivity ($d\rho/dT$) shown in Fig. S2(b) [32], which is somewhat lower than that of CVT-grown samples [15, 34–36]. With S doping, T_s is gradually suppressed. For $x < 0.31$, $\text{FeSe}_{1-x}\text{S}_x$ single crystals exhibit metallic behavior over the entire temperature range. Extending to higher doping levels, a resistive anomaly with a characteristic temperature, T^* , emerges and survives up to $x \sim 0.71$. Below T^* , the resistivity shows an anomalous upturn before the SC transition, as is clearly shown in Fig. 2(e) for a representative example with $x = 0.45$. Data for the other crystals can be seen in Fig. S2(c) [32]. T^* shows a nonmonotonic doping dependence, i.e., T^* initially increases and then decreases with S doping. It is noted that a similar resistivity upturn has also been recently observed in $\text{FeSe}_{1-x}\text{S}_x$ ($x \leq 0.43$) thin films [29], possibly due to a magnetic transition, as revealed in FeSe and $\text{FeSe}_{1-x}\text{S}_x$ single crystals under pressure [37–39].

Figure 2(b) shows an enlarged view of normalized $\rho(T)$ curves below $T = 50$ K. The SC transition temperature, T_c^{zero} , defined as the zero resistivity temperature, is indicated by red arrows. With increasing x , T_c^{zero} increases slightly from 8.4 K in FeSe to 9.6 K at $x \sim 0.11$ followed by a decrease to a minimum value of 2.8 K at $x = 0.45$. Then, T_c^{zero} gradually increases to 4.6 K in FeS ($x = 1$). Figure 2(c) shows the temperature dependence of the zero-field-cooled (ZFC) magnetization under an applied magnetic field of 5 Oe. T_c^{M} is defined as the

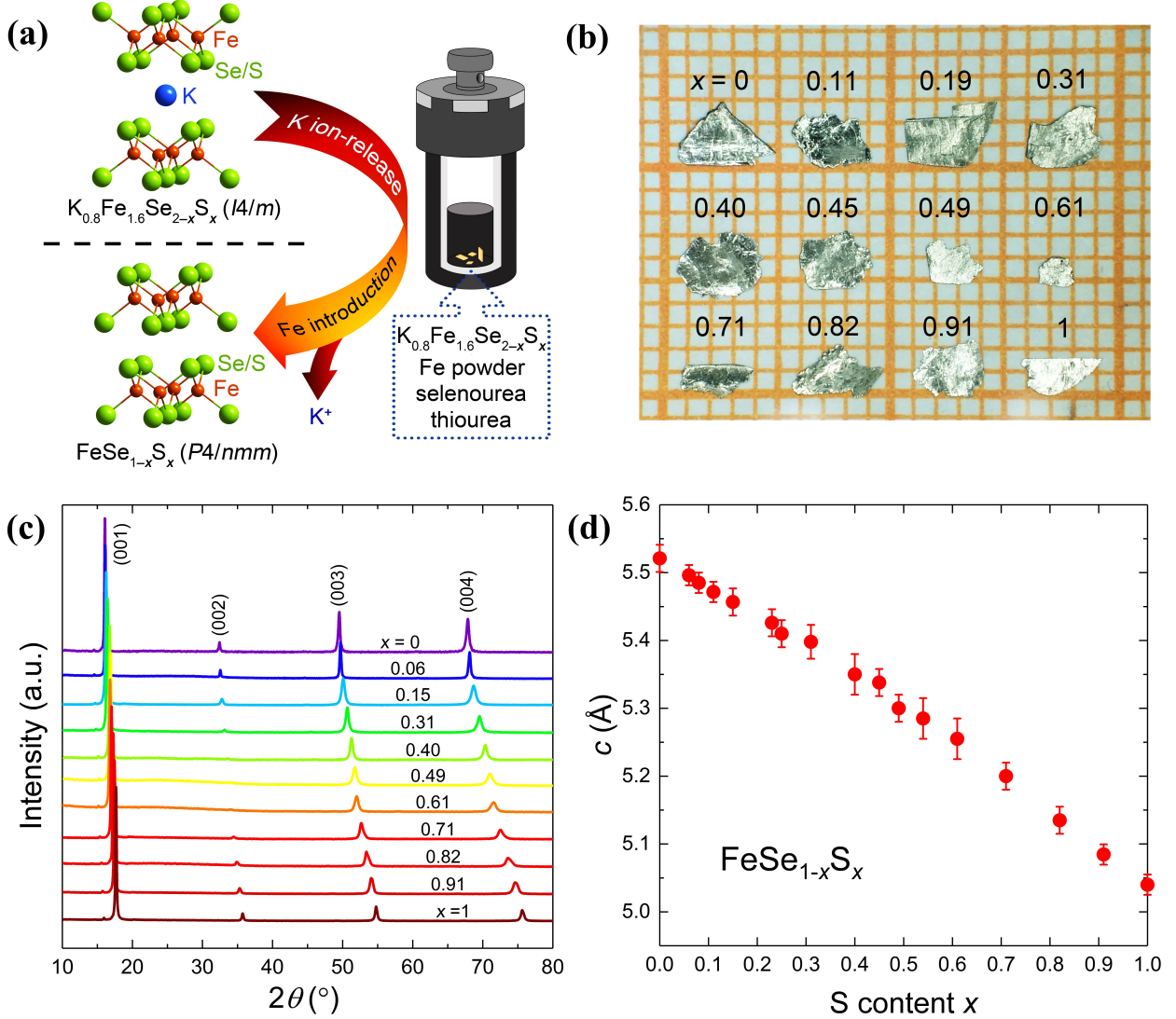


FIG. 1. (a) Schematic illustration of the hydrothermal ion release/introduction route for the synthesis of $\text{FeSe}_{1-x}\text{S}_x$ single crystals. (b) Optical image of select $\text{FeSe}_{1-x}\text{S}_x$ single crystals. (c) Single-crystal XRD patterns of $\text{FeSe}_{1-x}\text{S}_x$ single crystals with various values of x . All (00 l) peaks obviously shift to higher angles with increasing x , indicative of effective S doping. (d) Lattice parameter c deduced from the XRD patterns as a function of S content, x .

onset of diamagnetism, which is almost consistent with the T_c^{zero} value determined from the resistivity measurements.

To gain more insight into the effect of doping on the normal state transport properties, particularly in the S doping region with $x > 0.25$, we analyzed the normal state resistivity below $T = 50$ K by fitting the results to a power law $\rho(T) = \rho_0 + AT^n$, where ρ_0 is the residual resistivity at zero temperature and n is the temperature exponent [40–42]. For $0.31 \leq x \leq 0.71$, the fits are performed in the temperature region of $T^* + 10$ K to 50 K to minimize the effect of upturn behavior. The fitting curves are represented by black dotted lines in Fig. 2(b). The obtained exponent n and residual resistivity ρ_0 are

plotted in Fig. 2(d). In addition, the RRR value, which is defined as $\rho(300 \text{ K})/\rho_0$ and describes the strength of disorder scattering in samples, is also shown in Fig. 2(d). The RRR firstly decreases from 17 in undoped FeSe single crystals to 6 at $x = 0.25$ (smaller than that of CVT-grown single crystals [19, 35, 36]). The ration slowly increases with further S doping and finally increases steeply to 48 for $x = 1$.

Typically, $n = 2$ is expected for a conventional metal described by the Landau Fermi-liquid theory, while a power law with $n < 2$ indicates non-Fermi-liquid behavior. As shown in Fig. 2(d), the exponent n maintains a nearly constant value slightly below 1 in the low-S doping region. The exponent then increases un-

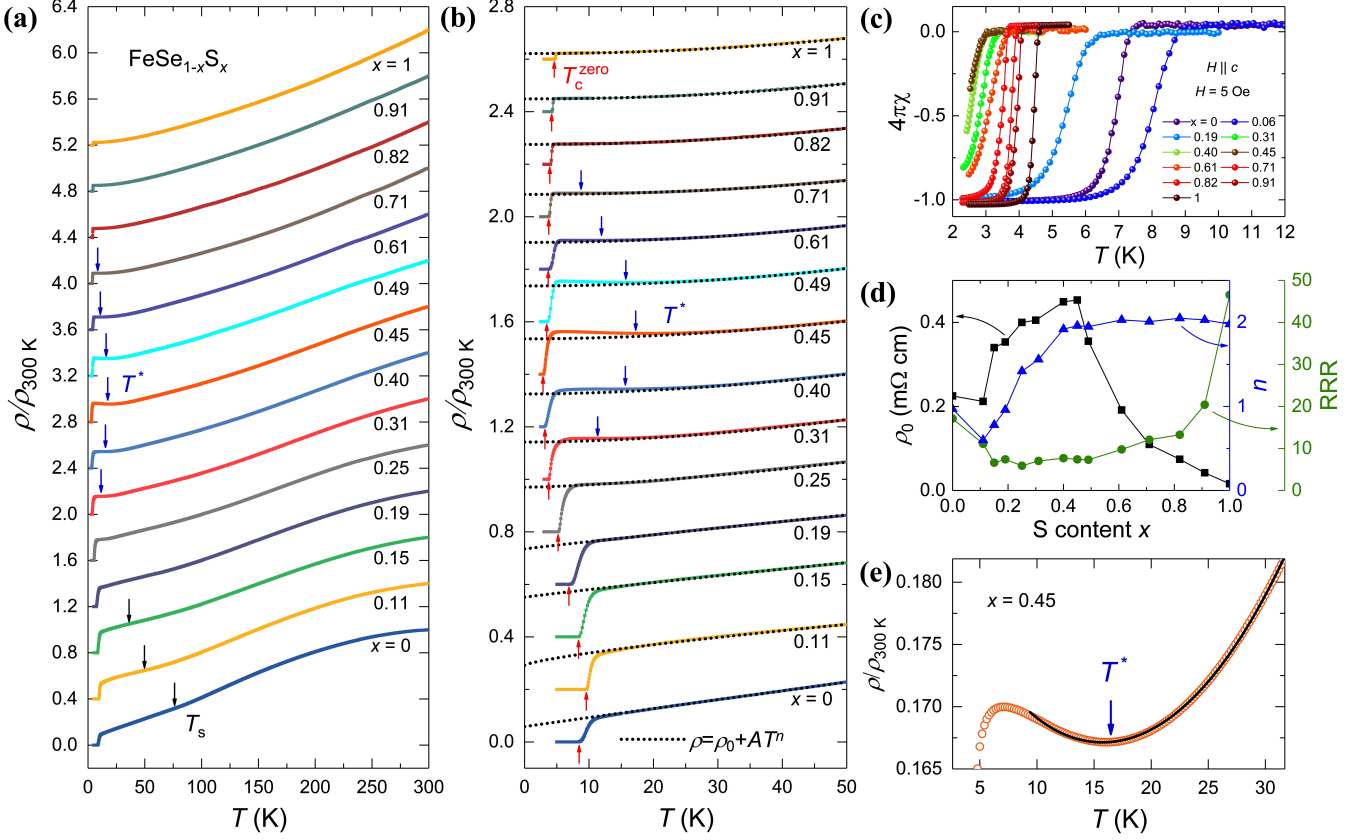


FIG. 2. (a) Temperature dependence of the in-plane resistivity (normalized by corresponding values at $T = 300$ K) for FeSe_{1-x}S_x ($0 \leq x \leq 1$) single crystals. An enlarged view for temperatures below $T = 50$ K is shown in panel (b). The data are vertically shifted for clarity. The arrows indicate the nematic transition at T_s , resistivity minimum at T^* , and SC transition at T_c^{zero} . The black dotted lines in panel (b) represent fits to the formula $\rho(T) = \rho_0 + AT^n$ (see text for details). (c) Temperature dependence of ZFC magnetization for FeSe_{1-x}S_x single crystals under 5 Oe with $H \parallel c$ -axis. (d) Residual resistivity ρ_0 , temperature exponent n , and residual resistivity ratio (RRR) as a function of S content, x . (e) An enlarged view of the normalized resistivity of a typical FeSe_{1-x}S_x single crystal with $x = 0.45$ near the resistivity upturn region. The black solid line is a fit to the formula $\rho(T) = \rho_0 + AT^n + C\ln(T^*/T)$.

til saturating at 2 with increasing x , indicating an evolution from non-Fermi-liquid to Fermi-liquid transport. This evolution can be more clearly seen in a contour plot of the temperature-dependent n extracted from $\ln(\rho - \rho_0)/\ln T$ in Fig. 3(a). The resistivity shows a sublinear temperature dependence in the nematic phase. Outside the nematic phase, a dominant $T^{1.5}$ dependence is visible at high temperatures, and a Fermi-liquid behavior is recovered with decreasing temperature at low temperatures. This $T^{1.5}$ dependence was also observed in the CVT-grown single crystals with $x \leq 0.25$ [21]. As x increases further, the Fermi-liquid region observed at low temperatures extends to higher temperatures.

In contrast, in the Fermi-liquid region with $\rho(T) = \rho_0 + AT^2$, the coefficient A is proportional to the carrier's effective mass, i.e., $A \propto (m^*/m_0)^2$. Thus, we replotted the $\rho(T)$ data for $x \geq 0.25$ in the form of ρ versus T^2 , as shown in Fig. S3 [32]. The coefficient A obtained from a linear fitting to low temperatures is presented in Fig.

3(a). Clearly, A decreases monotonically with increasing x , signifying a reduction in effective mass with S doping. Indeed, angle-resolved photoemission spectroscopy indicates that the electronic correlations are suppressed by S doping in FeSe_{1-x}S_x single crystals toward FeS, as evidenced by an increased Fermi velocity and bandwidth [43].

Next, we turn our attention to the resistivity upturn at T^* . Considering the relatively small RRR values in our hydrothermal single crystals, one would expect that the resistivity upturn at low temperatures might be ascribed to the weak localization effect originating from the presence of disorder potentials. In this case, the resistivity should exhibit logarithmic temperature dependence, as has been well observed in two-dimensional electron system [44]. Considering the weak localization effect, the resistivity can be expressed as $\rho(T) = \rho_0 + AT^n + C\ln(T^*/T)$, where A and C are constants and T^* is the characteristic temperature at which

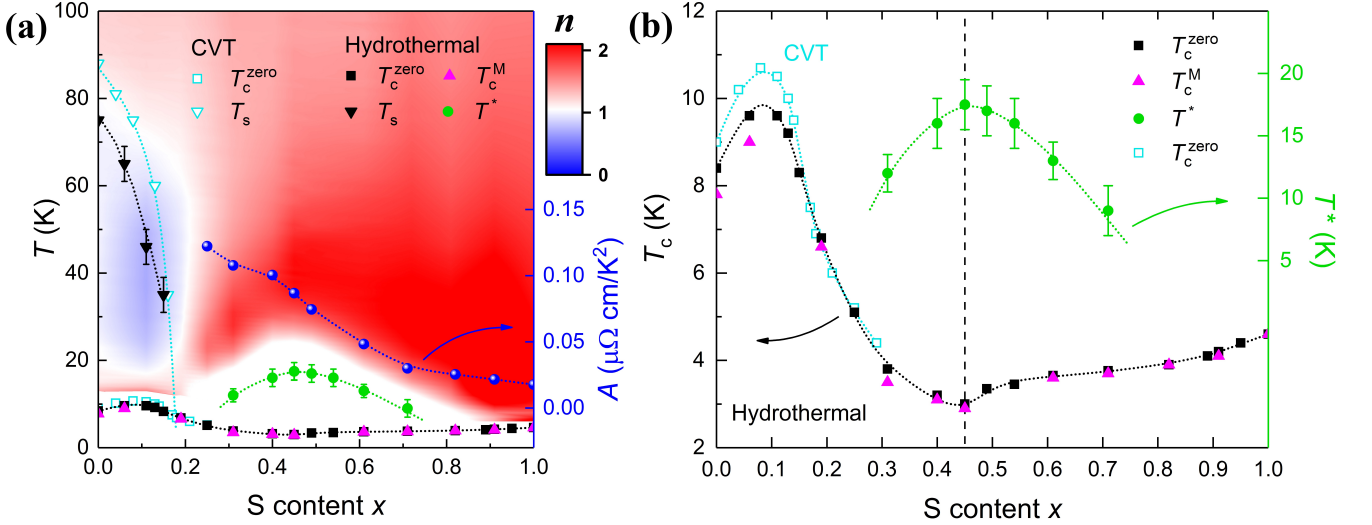


FIG. 3. (a) Complete phase diagram of hydrothermal $\text{FeSe}_{1-x}\text{S}_x$ single crystals in the present study. T_s represents the nematic transition temperature. T_c^{zero} and T_c^{M} are the SC transition temperatures obtained from resistivity and magnetization measurements, respectively. T^* is the characteristic temperature at which the $\rho-T$ curves show local minimum at low temperatures. For comparison, corresponding data for CVT-grown $\text{FeSe}_{1-x}\text{S}_x$ ($0 \leq x \leq 0.29$) single crystals reported in Refs. [15, 16, 21] are also included. The temperature dependence of the exponent n extracted from $\text{dln}(\rho - \rho_0)/\text{dln}T$ for each crystal is represented as a contour map (see text). The coefficient A is obtained by fitting the low-temperature resistivity using the Fermi-liquid formula $\rho(T) = \rho_0 + AT^2$ (see Fig. S3 [32]). (b) Enlarged view of T_c and T^* as a function of S content, x .

the resistivity reaches a local minimum, as proposed in Ref. [41]. To confirm the validity of this model, we fit the experimental data at low temperatures, as represented by solid lines in Fig. 2(e) and Fig. S2(c) [32]. As can be seen, the fitting curves agree well with the experimental data except for some small deviations close to T_c due to the effect of SC fluctuations. In the scenario of a weak localization effect, disorder-induced localization would lead to a more profound resistivity upturn or a higher T^* with increasing disorder. In the crystal with an x value of approximately 0.5, the disorder effect would be the strongest due to the largest lattice mismatch in the Se/S layer. Indeed, the single crystal with $x = 0.45$ exhibits the largest T^* , which is consistent with the expectation for the weak localization scenario. This evolution of disorder is also reflected by the residual resistivity ρ_0 , as presented in Fig. 2(d), which shows a trend similar to that of T^* . Moreover, we note that a resistivity upturn also occurs in polycrystalline $\text{FeSe}_{0.5}\text{S}_{0.5}$ samples [45] and thin flakes of FeSe with a thickness of 9 nm [46], which show a smaller RRR and increased disorder and local inhomogeneities. Therefore, we tentatively attribute the resistivity upturn to the disorder-induced weak localization effect.

Based on the resistivity and magnetization data, we constructed complete phase diagram of $\text{FeSe}_{1-x}\text{S}_x$ single crystals, as shown in Fig. 3(a). For comparison, corresponding data obtained from the CVT-grown $\text{FeSe}_{1-x}\text{S}_x$ ($0 \leq x \leq 0.29$) single crystals reported in Refs. [15, 16, 21] are also included. With isovalent S

doping, the nematic transition is found to be gradually suppressed and finally vanishes at $x \sim 0.17$. However, the superconductivity is robust against S doping and spans the entire doping region of $0 \leq x \leq 1$. To more clearly present the evolution of T_c with S doping, we redrew the phase diagram at low temperatures, as shown in Fig. 3(b). Within the nematic phase, a small dome-shaped SC phase is observed, consistent with previous results for CVT-grown single crystals [14–17]. It is noted that the values of both T_s and T_c in our hydrothermal single crystals are slightly lower than those of CVT-grown single crystals. Böhmer *et al.* have argued that the reduction of both T_s and T_c correlates with decreasing RRR values, i.e., the disorder effect [35].

Outside the nematic phase, the superconductivity is continuously suppressed, leading to a minimum $T_c = 2.8$ K at $x = 0.45$; beyond this point, T_c slowly increases to 4.6 K at $x = 1$. It has been reported that the SC gap exhibits an abrupt change across the nematic QCP ($x \sim 0.17$), suggesting that the pairing mechanism may be different inside (denoted as SC1) and outside (denoted as SC2) the nematic phase [19, 20]. For $x > 0.45$, the trend of T_c suddenly reverses, and T_c slowly increases toward FeS, indicating that the SC phase at $x > 0.45$ may be different from that of SC2. A similar minimum T_c has also been observed in the middle of the phase diagram for other IBSSs. In 1111-type LaFeAsO , a second SC dome has been reported at high doping levels upon substitution of O with F or H [47, 48]. For 122-type KFe_2As_2 , T_c first decreases and then increases with increasing pres-

sure, exhibiting a V-shaped behavior, which may indicate a pairing symmetry change [49, 50].

Another remarkable feature of this phase diagram is the evolution of T^* with S doping, which exhibits dome-like behavior with a maximum value of 17.5 K at $x = 0.45$. T^* has also been observed in $\text{FeSe}_{1-x}\text{S}_x$ ($x \leq 0.43$) thin films, emerging just after the disappearance of the nematic phase at $x \sim 0.18$ and increasing monotonically to $x = 0.43$ [29]. In our single crystals, T^* initially appears at $x = 0.31$, and its magnitude is smaller than that of thin films [29]. Such differences may be due to the strain effect in thin films. Interestingly, the evolution of T^* is opposite to that of T_c , reflecting competition between T_c and T^* . As discussed above, the weak localization effect due to disorder-related scattering may be the origin of T^* . In this case, T_c should increase when the weak localization effect is suppressed, which is in agreement with our results. Recent studies on Te-doped $\text{FeSe}_{1-x}\text{Te}_x$ single crystals have demonstrated a broad minimum of T_c near $x \sim 0.2$, which may also be attributed to the effect of disorder, although no obvious resistivity upturn has been observed [51].

It has been suggested that the resistivity upturn in $\text{FeSe}_{1-x}\text{S}_x$ ($x \leq 0.43$) thin films may be associated with a possible magnetic transition [29], which is somewhat reminiscent of the behavior of FeSe and $\text{FeSe}_{1-x}\text{S}_x$ single crystals under pressure [37, 38]. It has been demonstrated that the increase in chalcogen height h_{Ch} may be responsible for the emergence of magnetic order in pressurized $\text{FeSe}_{1-x}\text{S}_x$ single crystals [52]. However, in contrast to the physical pressure results, h_{Ch} decreases monotonically upon isovalent S doping. As a consequence, the magnetic order shifts to higher pressures with increasing S content, as higher pressures are required for obtaining a larger h_{Ch} to induce magnetic order [38]. In this sense, it may be difficult to stabilize the magnetic order by S doping at ambient pressure. Moreover, aside from the magnetism observed at high pressures [37, 38], an additional low-pressure magnetic dome has also been detected in $\text{FeSe}_{1-x}\text{S}_x$ single crystals [53, 54]. This magnetic order competes with superconductivity at low pressures, which leads to a local maximum in T_c , where the magnetic order arises. It has been found that the local maximum in T_c shifts to lower pressures with increas-

ing S doping, indicating the possible coexistence of superconductivity and magnetism in $\text{FeSe}_{1-x}\text{S}_x$ at ambient pressure for $x \geq 0.2$ [54]. Further theoretical and experimental investigations are highly desired to clarify the origin of T^* and its relation to the magnetic transition.

IV. CONCLUSION

In conclusion, we have synthesized a series of $\text{FeSe}_{1-x}\text{S}_x$ ($0 \leq x \leq 1$) single crystals by a hydrothermal method and have constructed a complete phase diagram based on resistivity and magnetization data. In the low-S doping region, the phase diagram is consistent with that of CVT-grown single crystals. Outside the nematic phase, the superconductivity is continuously suppressed and reaches a minimum T_c at $x = 0.45$; beyond this point, T_c slowly increases to $x = 1$. Remarkably, a resistivity upturn above T_c associated with a characteristic temperature T^* is observed, which exhibits a dome shape with a maximum value at $x = 0.45$, indicative of competition between T_c and T^* . Weak localization effect or a possible magnetic transition may be responsible for the resistivity anomaly at T^* . Certainly, different approaches such as Mössbauer, NMR, and neutron scattering experiments are warranted to clarify whether the resistivity anomaly is associated with magnetic order.

ACKNOWLEDGMENTS

This work was partly supported by the National Key R&D Program of China (Grant No. 2018YFA0704300), the Strategic Priority Research Program (B) of the Chinese Academy of Sciences (Grant No. XDB25000000) and the National Natural Science Foundation of China (Grant No. 11674054). X. Z. Xing was also supported by the Project funded by China Postdoctoral Science Foundation (Grant No. 2019M661679) and the Jiangsu Planned Projects for Postdoctoral Research Funds (Grant No. 2019K149). Y. Sun was supported by JSPS KAKENHI (Grant Nos. JP20H05164 and JP19K14661).

Xiaolei Yi and Xiangzhuo Xing contributed equally to this work.

-
- [1] Y. Kamihara, T. Watanabe, M. Hirano, and H. Hosono, *J. Am. Chem. Soc.* **130**, 3296 (2008).
 - [2] F. C. Hsu, J. Y. Luo, K. W. Yeh, T. K. Chen, T. W. Huang, P. M. Wu, Y. C. Lee, Y. L. Huang, Y. Y. Chu, D. C. Yan, and M. K. Wu, *Proc. Natl. Acad. Sci. USA* **105**, 14262 (2008).
 - [3] T. Shibauchi, T. Hanaguri, and Y. Matsuda, *J. Phys. Soc. Jpn.* **89**, 102002 (2020).
 - [4] S. Medvedev, T. M. McQueen, I. A. Troyan, T. Palasyuk, M. I. Erements, R. J. Cava, S. Naghavi, F. Casper, V. Ksenofontov, G. Wortmann, and C. Felser, *Nat. Mater.* **8**, 630 (2009).
 - [5] X. F. Lu, N. Z. Wang, H. Wu, Y. P. Wu, D. Zhao, X. Z. Zeng, X. G. Luo, T. Wu, W. Bao, G. H. Zhang, F. Q. Huang, Q. Z. Huang, and X. H. Chen, *Nat. Mater.* **14**, 325-329 (2015).
 - [6] B. Lei, J. H. Cui, Z. J. Xiang, C. Shang, N. Z. Wang, G. J. Ye, X. G. Luo, T. Wu, Z. Sun, and X. H. Chen, *Phys. Rev. Lett.* **116**, 077002 (2016).
 - [7] C. H. Wen, H. C. Xu, C. Chen, Z. C. Huang, X. Lou, Y. J. Pu, Q. Song, B. P. Xie, M. Abdel-Hafiez, D. A. Chareev, A. N. Vasiliev, R. Peng, and D. L. Feng, *Nat.*

- Commun. **7**, 10840 (2016).
- [8] J. F. Ge, Z. L. Liu, C. Liu, C. L. Gao, D. Qian, Q. K. Xue, Y. Liu, and J. F. Jia, Nat. Mater. **14**, 285-289 (2015).
 - [9] Q.-Y. Wang, Z. Li, W.-H. Zhang, Z.-C. Zhang, J.-S. Zhang, W. Li, H. Ding, Y.-B. Ou, P. Deng, K. Chang, J. Wen, C.-L. Song, K. He, J.-F. Jia, S.-H. Ji, Y.-Y. Wang, L.-L. Wang, X. Chen, X.-C. Ma, and Q.-K. Xue, Chin. Phys. Lett. **29**, 037402 (2012).
 - [10] S. Kasahara, T. Watashige, T. Hanaguri, Y. Kohsaka, T. Yamashita, Y. Shimoyama, Y. Mizukami, R. Endo, H. Ikeda, K. Aoyama, T. Terashima, S. Uji, T. Wolf, H. von Lohneysen, T. Shibauchi, and Y. Matsuda, Proc. Natl. Acad. Sci. USA **111**, 16309 (2014).
 - [11] T. M. McQueen, A. J. Williams, P. W. Stephens, J. Tao, Y. Zhu, V. Ksenofontov, F. Casper, C. Felser, and R. J. Cava, Phys. Rev. Lett. **103**, 057002 (2009).
 - [12] S. H. Baek, D. V. Efremov, J. M. Ok, J. S. Kim, J. van den Brink, and B. Buchner, Nat. Mater. **14**, 210 (2015).
 - [13] A. E. Bohmer, T. Arai, F. Hardy, T. Hattori, T. Iye, T. Wolf, H. V. Lohneysen, K. Ishida, and C. Meingast, Phys. Rev. Lett. **114**, 027001 (2015).
 - [14] A. I. Coldea, arXiv:2009.05523 (2020).
 - [15] S. Hosoi, K. Matsuura, K. Ishida, H. Wang, Y. Mizukami, T. Watashige, S. Kasahara, Y. Matsuda, and T. Shibauchi, Proc. Natl. Acad. Sci. USA **113**, 8139-8143 (2016).
 - [16] P. Wiecki, K. Rana, A. E. Böhrmer, Y. Lee, S. L. Bud'ko, P. C. Canfield, and Y. Furukawa, phys. Rev. B **98**, 020507(R) (2018).
 - [17] A. I. Coldea, S. F. Blake, S. Kasahara, A. A. Haghighirad, M. D. Watson, W. Knafo, E. S. Choi, A. McCollam, P. Reiss, T. Yamashita, M. Bruma, S. C. Speller, Y. Matsuda, T. Wolf, T. Shibauchi, and A. J. Schofield, npj Quan. Mater. **4**, 2 (2019).
 - [18] M. D. Watson, T. K. Kim, A. A. Haghighirad, S. F. Blake, N. R. Davies, M. Hoesch, T. Wolf, and A. I. Coldea, Phys. Rev. B **92**, 121108(R) (2015).
 - [19] Y. Sato, S. Kasahara, T. Taniguchi, X. Xing, Y. Kasahara, Y. Tokiwa, Y. Yamakawa, H. Kontani, T. Shibauchi, and Y. Matsuda, Proc. Natl. Acad. Sci. USA **115**, 1227 (2018).
 - [20] T. Hanaguri, Y. Kohsaka, T. Machida, T. Watashige, S. Kasahara, T. Shibauchi, and Y. Matsuda, Sci. Adv. **4**, eaar6419 (2018).
 - [21] M. Bristow, P. Reiss, A. A. Haghighirad, Z. Zajicek, S. J. Singh, T. Wolf, D. Graf, W. Knafo, A. McCollam, and A. I. Coldea, Phys. Rev. Research **2**, 013309 (2020).
 - [22] W. K. Huang, S. Hosoi, M. Čulo, S. Kasahara, Y. Sato, K. Matsuura, Y. Mizukami, M. Berben, N. E. Hussey, H. Kontani, T. Shibauchi, and Y. Matsuda, Phys. Rev. Research **2**, 033367 (2020).
 - [23] S. Licciardello, J. Buhot, J. Lu, J. Ayres, S. Kasahara, Y. Matsuda, T. Shibauchi, and N. E. Hussey, Nature **567**, 213-217 (2019).
 - [24] Y. Sun, A. Park, S. Pyon, T. Tamegai, and H. Kitamura, Phys. Rev. B **96**, 140505(R) (2017).
 - [25] Y. Sun, S. Kittaka, S. Nakamura, T. Sakakibara, K. Irie, T. Nomoto, K. Machida, J. Chen, and T. Tamegai, Phys. Rev. B **96**, 220505(R) (2017).
 - [26] H. C. Xu, X. H. Niu, D. F. Xu, J. Jiang, Q. Yao, Q. Y. Chen, Q. Song, M. Abdel-Hafiez, D. A. Chareev, A. N. Vasiliev, Q. S. Wang, H. L. Wo, J. Zhao, R. Peng, and D. L. Feng, Phys. Rev. Lett. **117**, 157003 (2016).
 - [27] P. O. Sprau, A. Kostin, A. Kreisel, A. E. Böhrmer, V. Taufour, P. C. Canfield, S. Mukherjee, P. J. Hirschfeld, B. M. Andersen, and J. C. S. Davis, Science **357**, 75-80 (2017).
 - [28] S. Lederera, Y. Schattnerb, E. Berg, and S. A. Kivelson, Proc. Natl. Acad. Sci. USA **114**, 4905 (2017).
 - [29] F. Nabeshima, T. Ishikawa, K.-i. Oyanagi, M. Kawai, and A. Maeda, J. Phys. Soc. Jpn. **87**, 073704 (2018).
 - [30] X. Dong, K. Jin, D. Yuan, H. Zhou, J. Yuan, Y. Huang, W. Hua, J. Sun, P. Zheng, W. Hu, Y. Mao, M. Ma, G. Zhang, F. Zhou, and Z. Zhao, Phys. Rev. B **92**, 064515 (2015).
 - [31] D. Yuan, Y. Huang, S. Ni, H. Zhou, Y. Mao, W. Hu, J. Yuan, K. Jin, G. Zhang, X. Dong, and F. Zhou, Chin. Phys. B **25**, 077404 (2016).
 - [32] See Supplemental Material at xxxxx for additional data and analysis.
 - [33] C. K. H. Borg, X. Zhou, C. Eckberg, D. J. Campbell, S. R. Saha, J. Paglione, and E. E. Rodriguez, Phys. Rev. B **93**, 094522 (2016).
 - [34] D. Chareev, Y. Ovchencov, L. Shvanskaya, A. Kovalskii, M. Abdel-Hafiez, D. J. Trainer, E. M. Lechner, M. Iavarone, O. Volkova, and A. Vasiliev, CrystEngComm **20**, 2449 (2018).
 - [35] A. E. Böhrmer, V. Taufour, W. E. Straszheim, T. Wolf, and P. C. Canfield, Phys. Rev. B **94**, 024526 (2016).
 - [36] Y. Sun, S. Pyon, and T. Tamegai, Phys. Rev. B **93**, 104502 (2016).
 - [37] J. P. Sun, K. Matsuura, G. Z. Ye, Y. Mizukami, M. Shimozaawa, K. Matsubayashi, M. Yamashita, T. Watashige, S. Kasahara, Y. Matsuda, J. Q. Yan, B. C. Sales, Y. Uwatoko, J. G. Cheng, and T. Shibauchi, Nat. Commun. **7**, 12146 (2016).
 - [38] K. Matsuura, Y. Mizukami, Y. Arai, Y. Sugimura, N. Maejima, A. Machida, T. Watanuki, T. Fukuda, T. Yajima, Z. Hiroi, K. Y. Yip, Y. C. Chan, Q. Niu, S. Hosoi, K. Ishida, K. Mukasa, S. Kasahara, J. G. Cheng, S. K. Goh, Y. Matsuda, Y. Uwatoko, and T. Shibauchi, Nat. Commun. **8**, 1143 (2017).
 - [39] T. Terashima, N. Kikugawa, S. Kasahara, T. Watashige, T. Shibauchi, Y. Matsuda, T. Wolf, A. E. Böhrmer, F. Hardy, C. Meingast, H. v. Löhneysen, and S. Uji, J. Phys. Soc. Jpn. **84**, 063701 (2015).
 - [40] J. G. Analytis, H.-H. Kuo, R. D. McDonald, Mark-Wartenbe, P. M. C. Rourke, N. E. Hussey, and I. R. Fisher, Nat. Phys. **10**, 194 (2014).
 - [41] R. Zhang, D. Gong, X. Lu, S. Li, M. Laver, C. Niedermayer, S. Danilkin, G. Deng, P. Dai, and H. Luo, Phys. Rev. B **91**, 094506 (2015).
 - [42] S. Kasahara, T. Shibauchi, K. Hashimoto, K. Ikada, S. Tonegawa, R. Okazaki, H. Shishido, H. Ikeda, H. Takeya, K. Hirata, T. Terashima, and Y. Matsuda, Phys. Rev. B **81**, 184519 (2010).
 - [43] P. Reiss, M. D. Watson, T. K. Kim, A. A. Haghighirad, D. N. Woodruff, M. Bruma, S. J. Clarke, and A. I. Coldea, Phys. Rev. B **96**, 121103 (2017).
 - [44] P. A. Lee, and T. V. Ramakrishnan, Rev. Mod. Phys. **57**, 287-337 (1985).
 - [45] Y. Mizuguchi, F. Tomioka, S. Tsuda, T. Yamaguchi, and Y. Takano, J. Phys. Soc. Jpn. **78**, 074712 (2009).
 - [46] L. S. Farrar, M. Bristow, A. A. Haghighirad, A. McCollam, S. J. Bending, and A. I. Coldea, npj Quan. Mater. **5**, 29 (2020).

- [47] S. Iimura, S. Matsuishi, H. Sato, T. Hanna, Y. Muraba, S. W. Kim, J. E. Kim, M. Takata, and H. Hosono, *Nat. Commun.* **3**, 943 (2012).
- [48] J. Yang, R. Zhou, L.-L. Wei, H.-X. Yang, J.-Q. Li, Z.-X. Zhao, and G.-Q. Zheng, *Chin. Phys. Lett.* **32**, 107401 (2015).
- [49] F. F. Tafti, A. Juneau-Fecteau, M.-È. Delage, S. R. d. Cotret, J.-P. Reid, A. F. Wang, X.-G. Luo, X. H. Chen, N. Doiron-Leyraud, and L. Taillefer, *Nat. Phys.* **9**, 349 (2013).
- [50] V. Taufour, N. Foroozani, M. A. Tanatar, J. Lim, U. Kaluarachchi, S. K. Kim, Y. Liu, T. A. Lograsso, V. G. Kogan, R. Prozorov, S. L. Bud'ko, J. S. Schilling, and P. C. Canfield, *Phys. Rev. B* **89**, 220509(R) (2014).
- [51] K. Terao, T. Kashiwagi, T. Shizu, R. A. Klemm, and K. Kadowaki, *Phys. Rev. B* **100**, 224516 (2019).
- [52] C. Y. Moon, and H. J. Choi, *Phys. Rev. Lett.* **104**, 057003 (2010).
- [53] L. Xiang, U. S. Kaluarachchi, A. E. Böhmer, V. Taufour, M. A. Tanatar, R. Prozorov, S. L. Bud'ko, and P. C. Canfield, *Phys. Rev. B* **96**, 024511 (2017).
- [54] S. Hohenstein, J. Stahl, Z. Shermadini, G. Simutis, V. Grinenko, D. A. Chareev, R. Khasanov, J. C. Orain, A. Amato, H. H. Klauss, E. Morenzoni, D. Johrendt, and H. Luetkens, *Phys. Rev. Lett.* **123**, 147001 (2019).